Supporting information for

Hydroxyl-rich surface of $Ti_3C_2T_x$ for metal sulfides as high performance electrode materials for sodium/lithium storage

Qi Han[1, §], Yanli Zhou[1, §, *], Rong Du[1], Bo Xiao[c], Jianbo Cheng[c], Ming Zhang[1], Caifu Dong[1], Xueqin Sun[1], Fuyi Jiang[1,*] and Jian Yang[b,*]

[1] School of Environmental and Material Engineering, Yantai University, Yantai 264005, P.R. China

[b] Key Laboratory of Colloid and Interface Chemistry, Ministry of Education School of Chemistry and Chemical Engineering, Shandong University, Jinan 250100, P.R. China

[c] The Laboratory of Theoretical and Computational Chemistry, School of Chemistry and Chemical Engineering, Yantai University, Yantai 264005, P.R. China

[§]Qi Han and Yanli Zhou contribute equally to this work

*Corresponding author. E-mail: Yanli Zhou, zhouyanli@ytu.edu.cn; Fuyi Jiang, fyjiang@ytu.edu.cn; Jian Yang, yangjian@sdu.edu.cn

Supplementary Figures and Tables

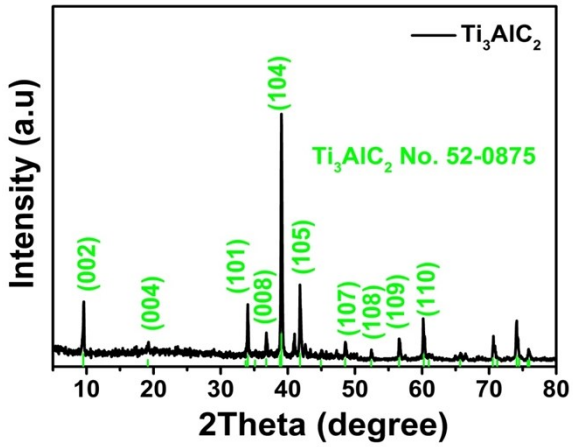

Fig. S1 XRD pattern of Ti_3AlC_2.

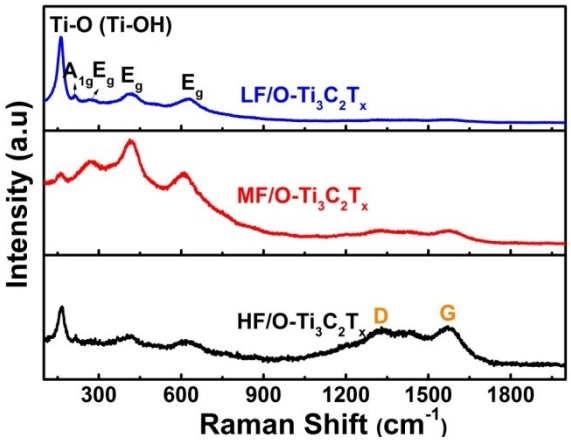

Fig. S2 Raman spectra of three $Ti_3C_2T_x$.

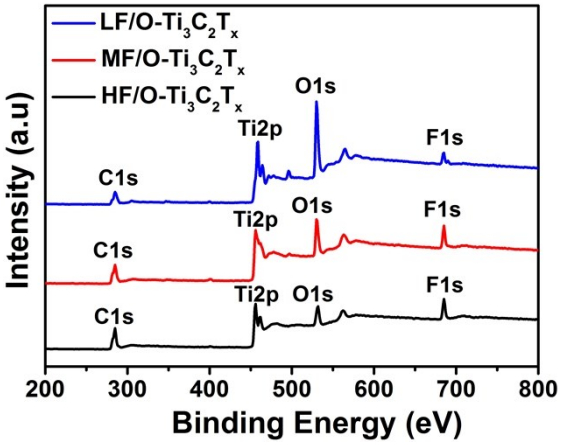

Fig. S3 XPS survey spectrum of three $Ti_3C_2T_x$.

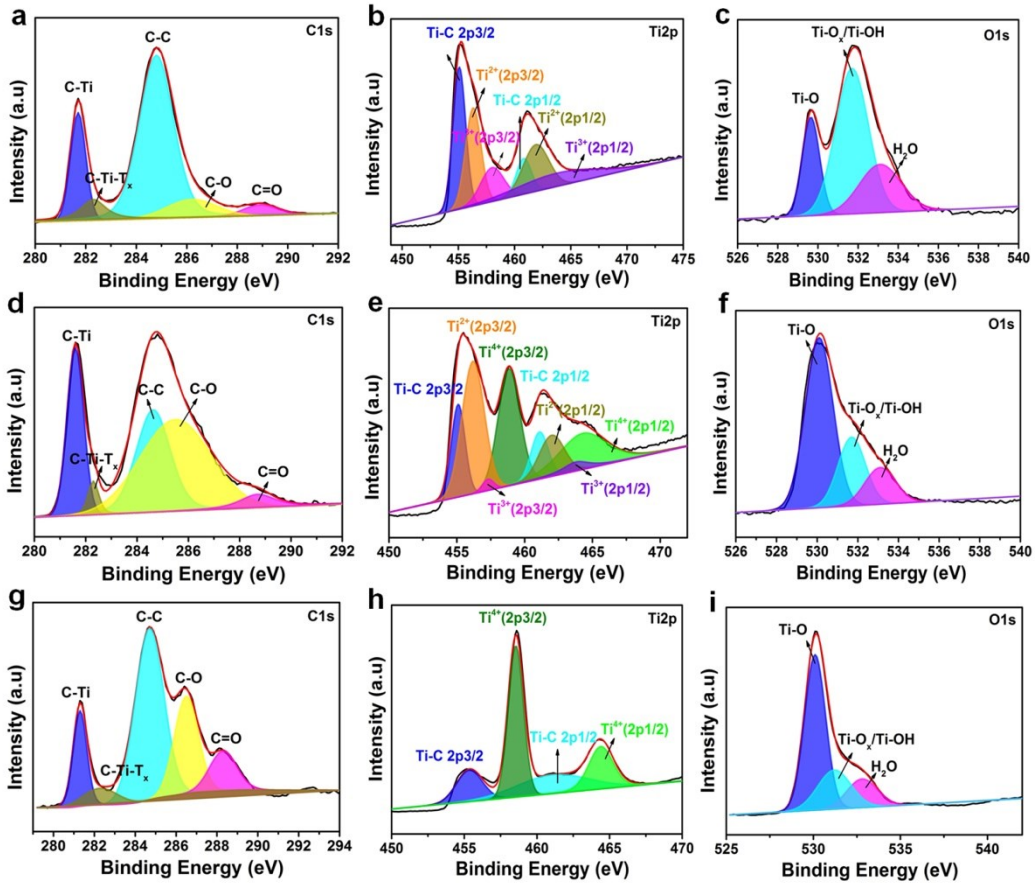

Fig. S4 XPS spectra of C1s, Ti2p and O1s for three titanium carbides：(a-c) HF/O-$Ti_3C_2T_x$, (d-f) MF/O-$Ti_3C_2T_x$ and (g-i) LF/O-$Ti_3C_2T_x$.

Table S1 The atomic ratio of three $Ti_3C_2T_x$ from EDS results.

Sample	*C-K*	*O-K*	*F-K*	*Al-K*	*Ti-K*
HF/O-$Ti_3C_2T_x$	**13.62**	**34.88**	**24.41**	**0.30**	**26.79**
MF/O-$Ti_3C_2T_x$	**16.98**	**41.88**	**18.75**	**0.13**	**22.26**
LF/O-$Ti_3C_2T_x$	**13.37**	**52.62**	**6.05**	**0.56**	**28.38**

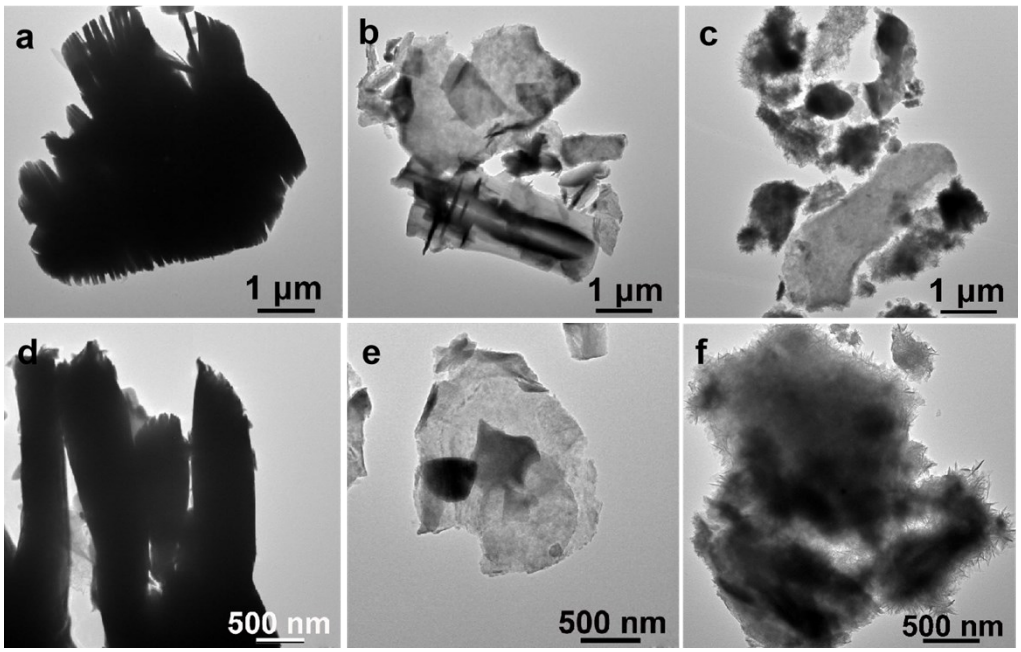

Fig. S5 TEM images of (a, d) HF/O-$Ti_3C_2T_x$, (b, e) MF/O-$Ti_3C_2T_x$, (c, f) LF/O-$Ti_3C_2T_x$.

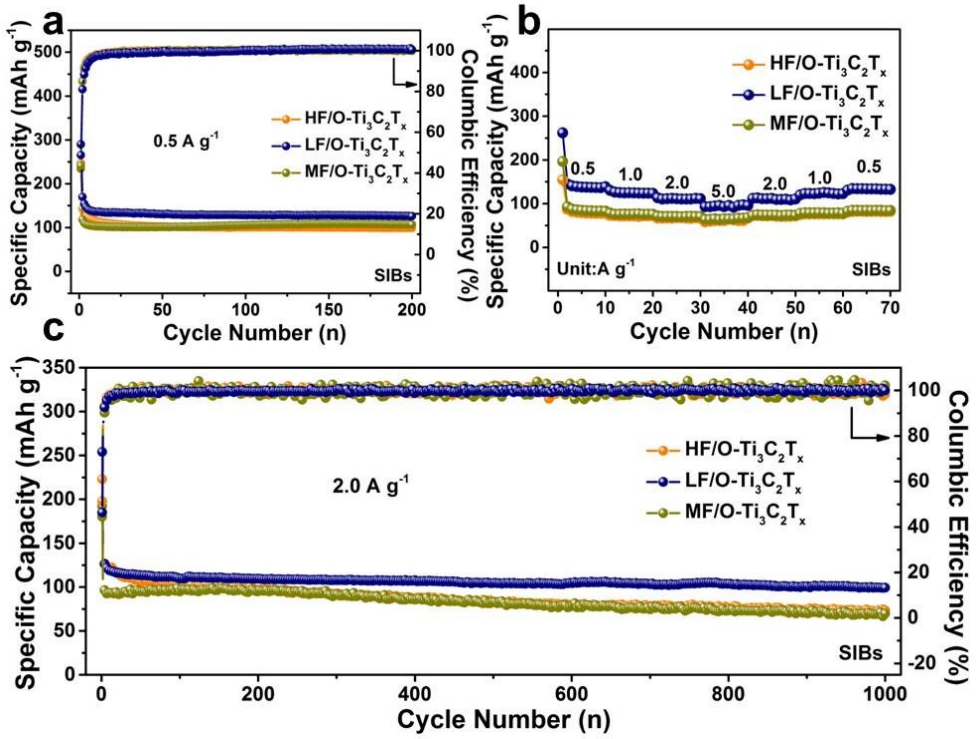

Fig. S6 (a) cycling performance at 0.5 A g^{-1}, (b) rate capabilities and (c) high-rate cycling performance of three $Ti_3C_2T_x$ for SIBs.

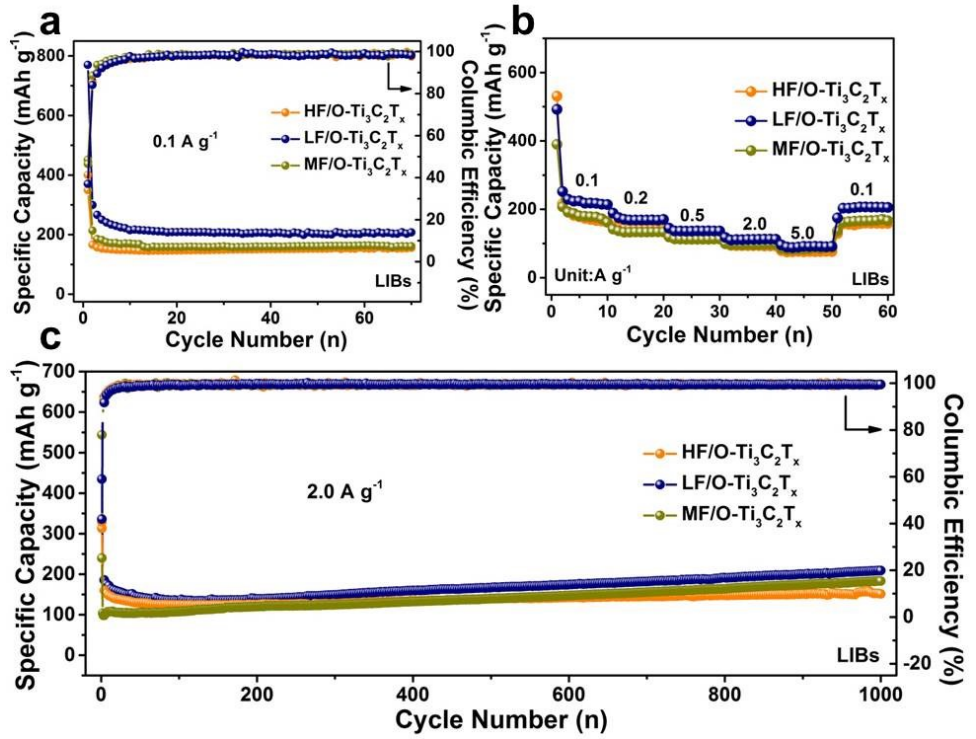

Fig. S7 (a) cycling performance at 0.1 A g^{-1}, (b) rate capabilities and (c) high-rate cycling performance of three $Ti_3C_2T_x$ for LIBs.

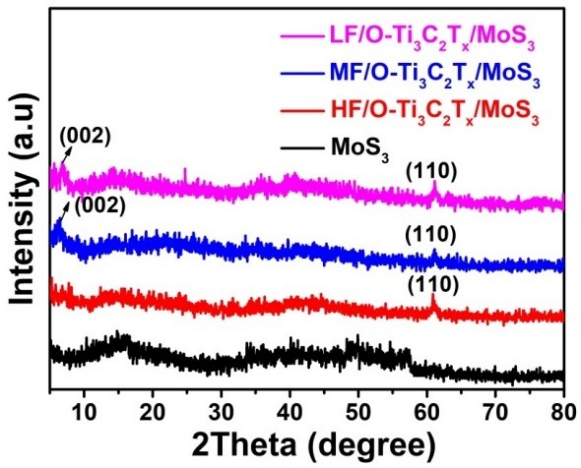

Fig. S8 XRD patterns of MoS_3, HF/O-$Ti_3C_2T_x$/MoS_3, MF/O-$Ti_3C_2T_x$/MoS_3 and LF/O-$Ti_3C_2T_x$/MoS_3.

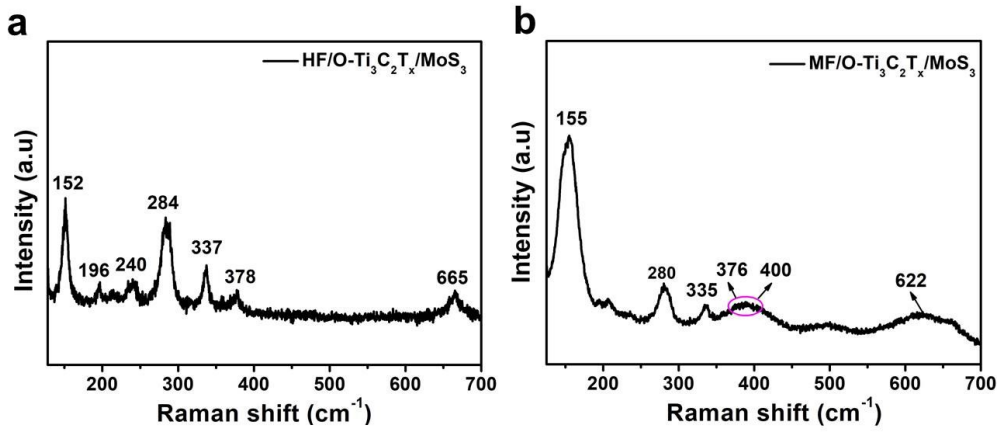

Fig. S9 Raman spectra of (a) HF/O-$Ti_3C_2T_x$/MoS_3 and (b) MF/O-$Ti_3C_2T_x$/MoS_3.

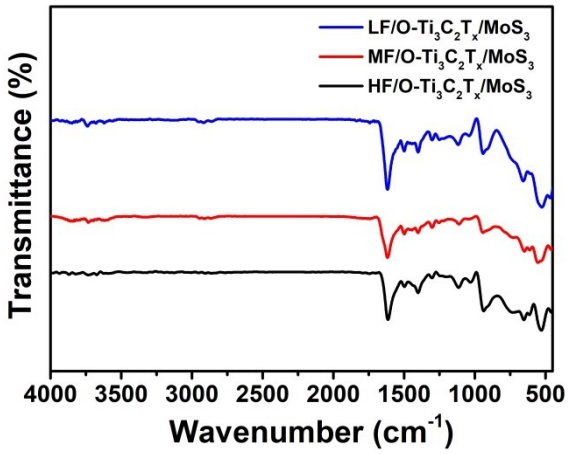

Fig. S10 FT-IR spectra of HF/O-$Ti_3C_2T_x$/MoS_3, MF/O-$Ti_3C_2T_x$/MoS_3 and LF/O-$Ti_3C_2T_x$/MoS_3.

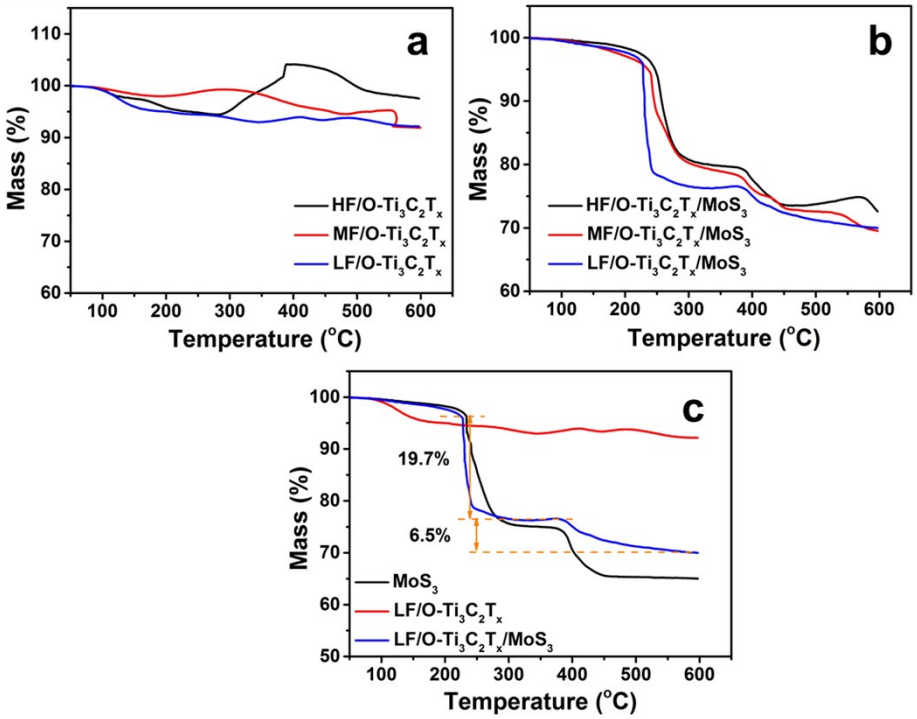

Fig. S11 TG curves of (a) three $Ti_3C_2T_x$, (b) three $Ti_3C_2T_x$/MoS_3 composites, (c) pure MoS_3, LF/O-$Ti_3C_2T_x$ and LF/O-$Ti_3C_2T_x$/MoS_3.

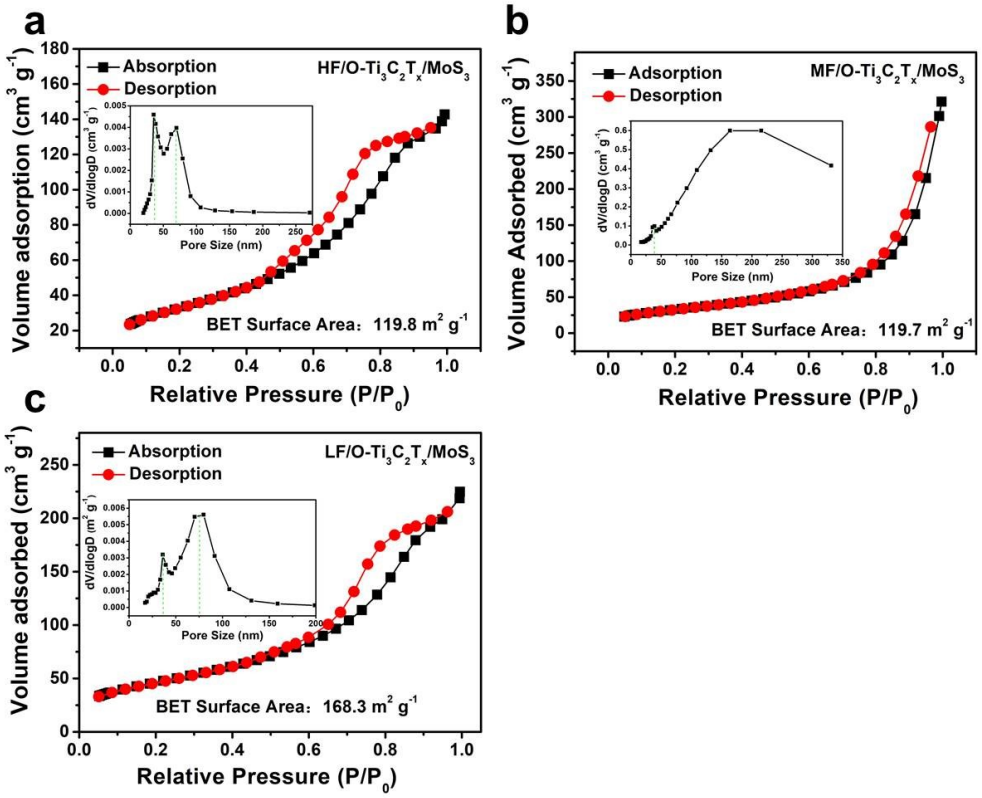

Fig. S12 N_2 adsorption-desorption isotherm and pore size distribution of (a) HF/O-$Ti_3C_2T_x/MoS_3$, (b) MF/O-$Ti_3C_2T_x/MoS_3$ and (c) LF/O-$Ti_3C_2T_x/MoS_3$.

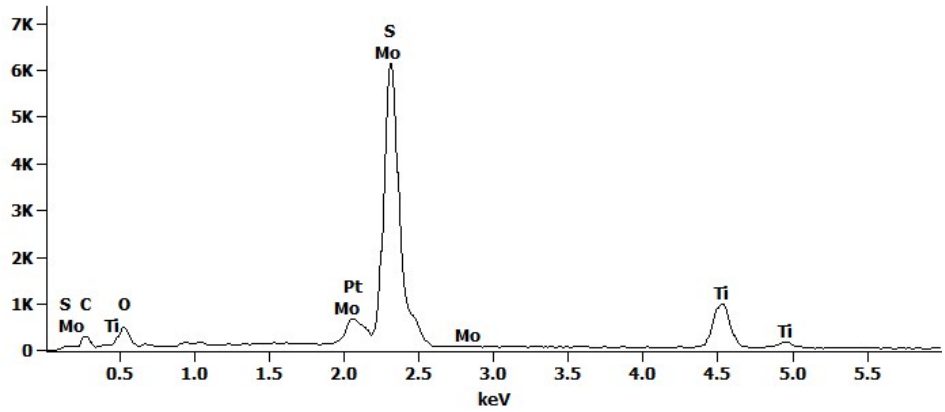

Fig. S13 EDS spectrum of LF/O-$Ti_3C_2T_x/MoS_3$.

Table S2 EDS result of LF/O-$Ti_3C_2T_x/MoS_3$.

	C-K	*O-K*	*S-K*	*Ti-K*	*Mo-L*	*Pt-M*
Atomic ratio	17.33	26.75	30.52	14.18	9.76	1.46
Mass ratio	5.92	12.18	27.84	19.33	26.65	8.08

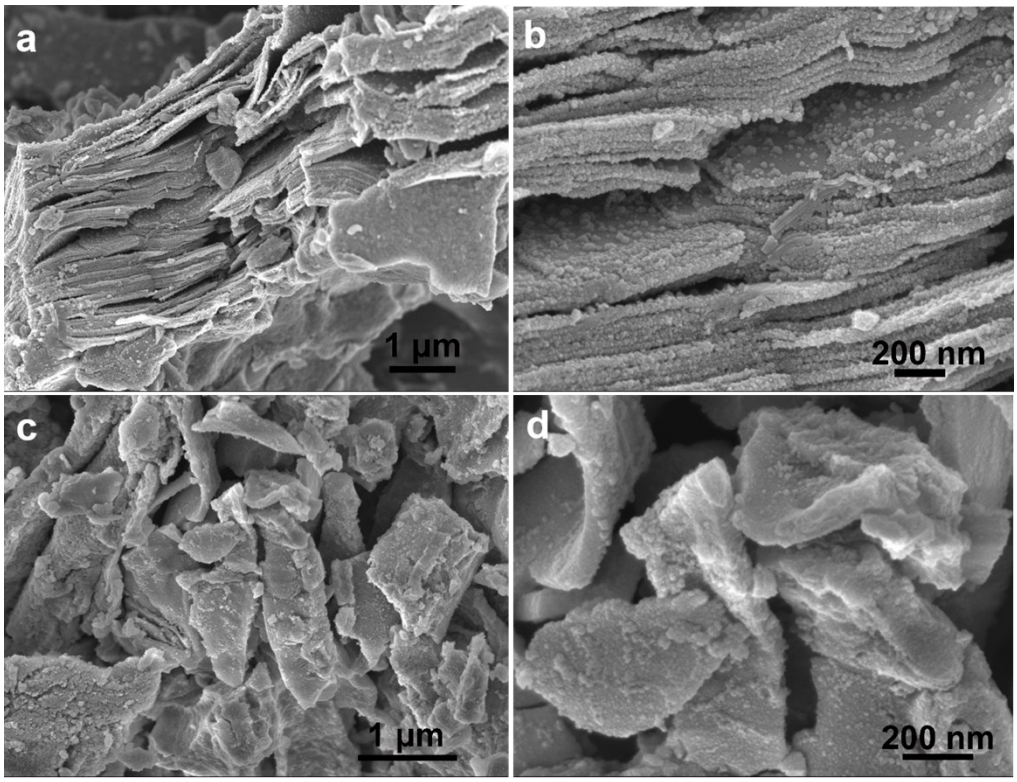

Fig. S14 Low magnified and high magnified SEM images of (a, b) HF/O-$Ti_3C_2T_x/MoS_3$, (c, d) MF/O-$Ti_3C_2T_x/MoS_3$.

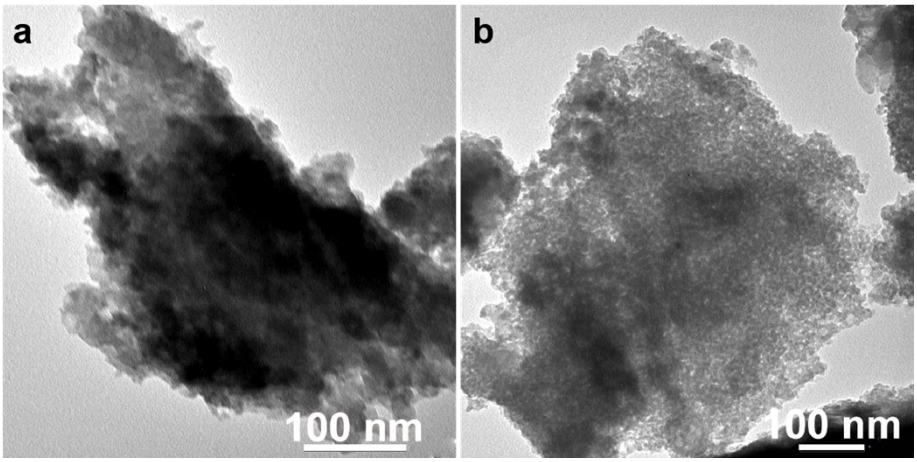

Fig. S15 TEM images of (a) HF/O-$Ti_3C_2T_x$/MoS_3, (b) MF/O-$Ti_3C_2T_x$/MoS_3.

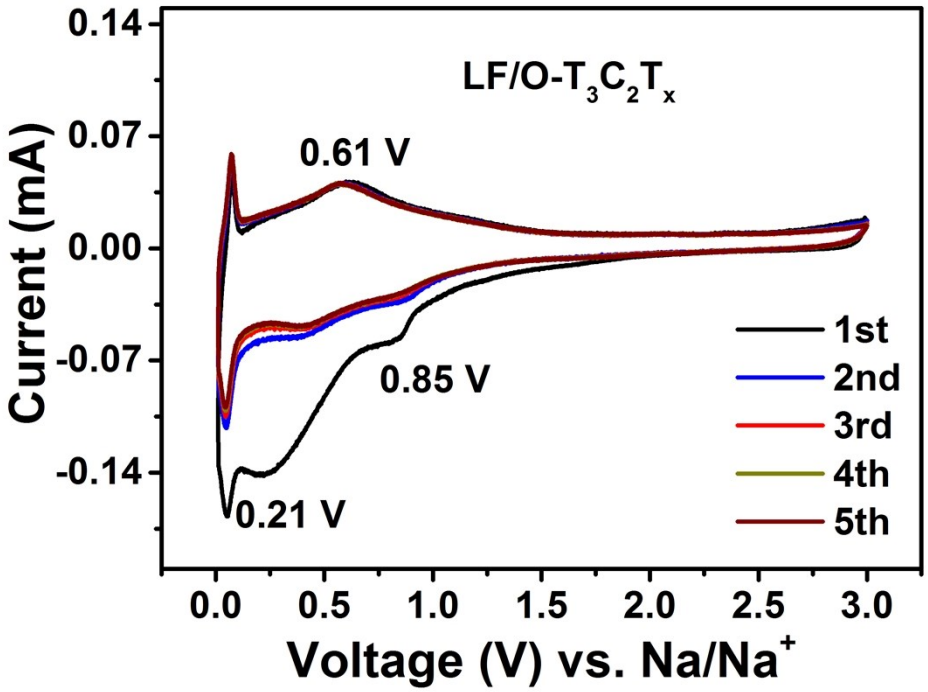

Fig. S16 CV curves of LF/O-$Ti_3C_2T_x$ for the first five cycles for SIBs.

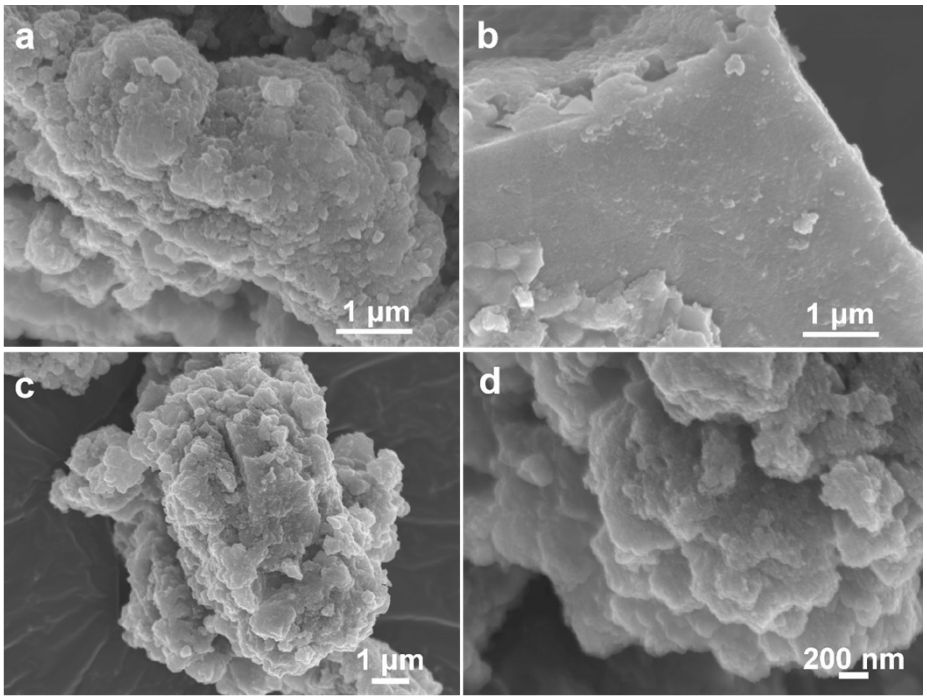

Fig. S17 SEM images of cycled electrodes: (a) HF/O-$Ti_3C_2T_x$/MoS_3, (b) MF/O-$Ti_3C_2T_x$/MoS_3, (c, d) LF/O-$Ti_3C_2T_x$/MoS_3.

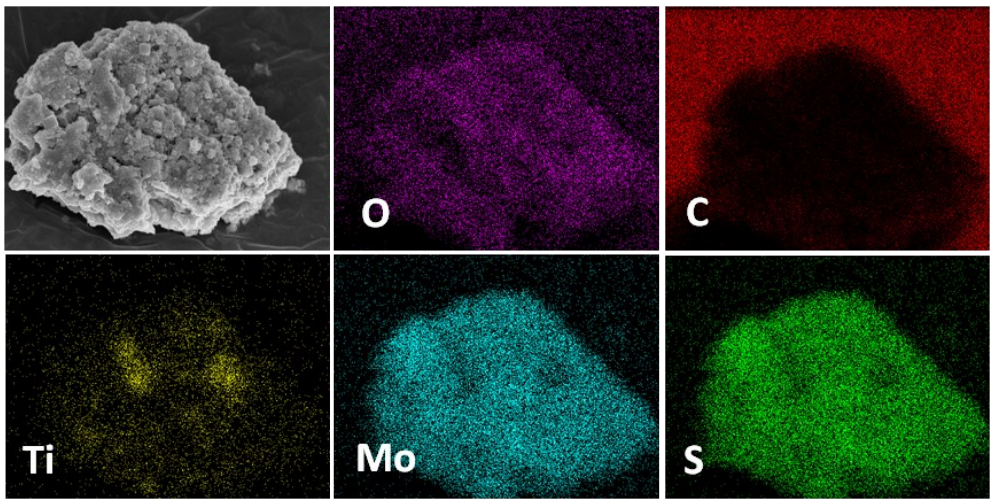

Fig. S18 SEM element mapping of cycled LF/O-$Ti_3C_2T_x$/MoS_3 electrode.

Table S3 The sodium storage performance comparison of molybdenum sulfide related composites.

Samples	Current density (mA g^{-1})	Cycle numbers	Specific capacity (mAh g^{-1})	Ref.
$(MoS_2/CF)@MoS_2@C$	100	200	773	[22]
	1000	1000	332	
MoS_2/rGO papers	25	20	230	[25]
DP-MoS_2	500	200	300	[28]
	2000	500	220	
LTO/MoS_2	2000	200	101	[S1]
amorphous MoS_3	2000	500	493	[S2]
Bi_2S_3/MoS_2	500	100	427	[S3]
MoS_2/NCF-MP	100	100	480	[S4]
	1000	300	390	
MoS_2 -CCNCs	100	100	385	[S5]
	2000	1000	298	
3D MoS_2 MFs	200	100	500	[S6]
$MoS_2@C@MoS_2$	100	100	434	[S7]
	1000	200	352	
HMF-MoS_2	100	100	384	[S8]
	1000	125	267	
MoS_2/G	100	60	432	[S9]
	300	250	441	
$C@MoS_2@PPy$	100	100	713	[S10]
	5000	500	294	
LF/O-$Ti_3C_2T_x/MoS_3$	500	180	973	This work
	2000	1000	611	

Table S4 Interaction energies, charge transfers and distances between MXenes and MoS_3.

	Interaction energy (eV)	Charge transfer (e)	Distance (Å)
$Ti_3C_2F_2 + MoS_3$	-0.05	-0.11	3.10
$Ti_3C_2O_2 + MoS_3$	-0.48	-0.57	2.85
$Ti_3C_2(OH)_2 + MoS_3$	-4.93	1.96	1.81

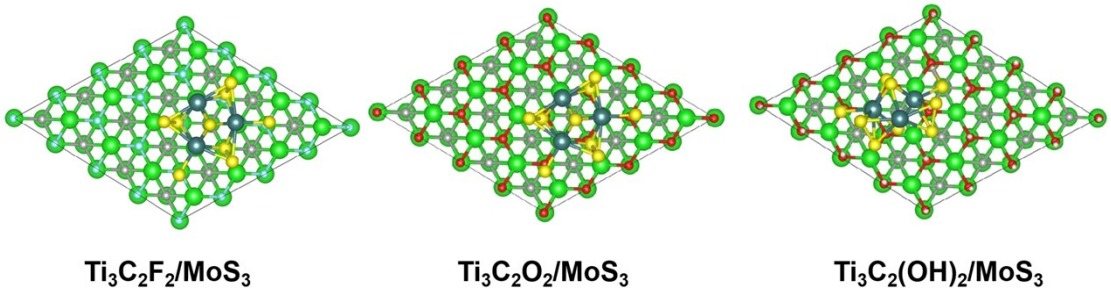

Fig. S19 Top views of the most stable adsorption structures for MoS_3 on $Ti_3C_2F_2$, $Ti_3C_2O_2$ and $Ti_3C_2(OH)_2$.

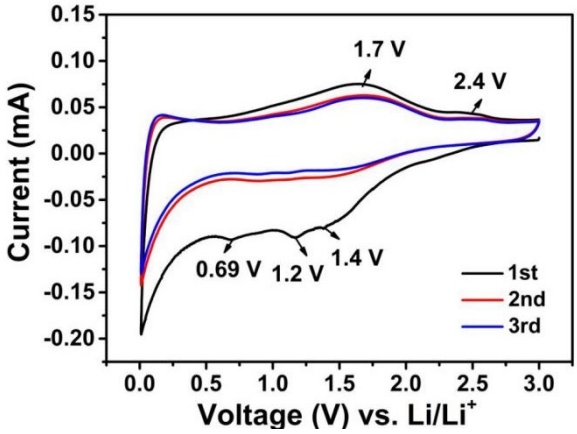

Fig. S20 CV curves of LF/O-$Ti_3C_2T_x$ for the first three cycles for LIBs.

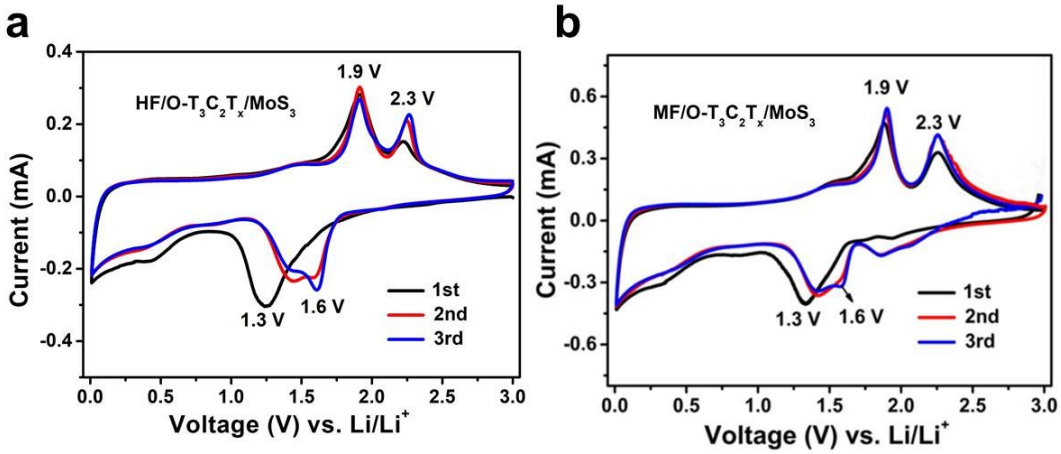

Fig. S21 CV curves of (a) HF/O-$Ti_3C_2T_x$/MoS_3, (b) MF/O-$Ti_3C_2T_x$/MoS_3 for LIBs.

Table S5 The lithium storage performance comparison of $Ti_3C_2T_x$ related composites.

Samples	Current density ($mA\ g^{-1}$)	Cycle numbers	Specific capacity ($mAh\ g^{-1}$)	Ref.
s-$Ti_3C_2T_x$/ Fe_3O_4	100	100	450	[35]
	2000	1000	327	
$Ti_3C_2T_x$/CNTs	500	500	287	[S11]
CNTs@$Ti_3C_2T_x$	1000	200	408	[S12]
CNFs/$Ti_3C_2T_x$	300	1800	320	[S13]
MoS_2/$Ti_3C_2T_x$	100	70	614	[S14]
RGO/$Ti_3C_2T_x$	500	200	150	[S15]
Fe_3O_4@Ti_3C_2	600	800	278	[S16]
SnO_2/Ti_3C_2	100	200	360	[S17]
Bi_2MoO_6/MXene	100	200	692	[S18]
	1000	1000	545	
Red P/$Ti_3C_2T_x$	200	600	585	[S19]
Co_3O_4@MF/O-$Ti_3C_2T_x$	1000	700	550	[S20]
Li_3VO_4/$Ti_3C_2T_x$	2000	1000	146	[S21]
SnS/Ti_3C_2	100	100	646	[S22]
$CoFeO_4$/$Ti_3C_2T_x$	900	100	200	[S23]
Co_3O_4 QDs/MXene	100	100	758	[S24]
LF/O-$Ti_3C_2T_x$/MoS_3	100	100	915	This work
	2000	1000	502	

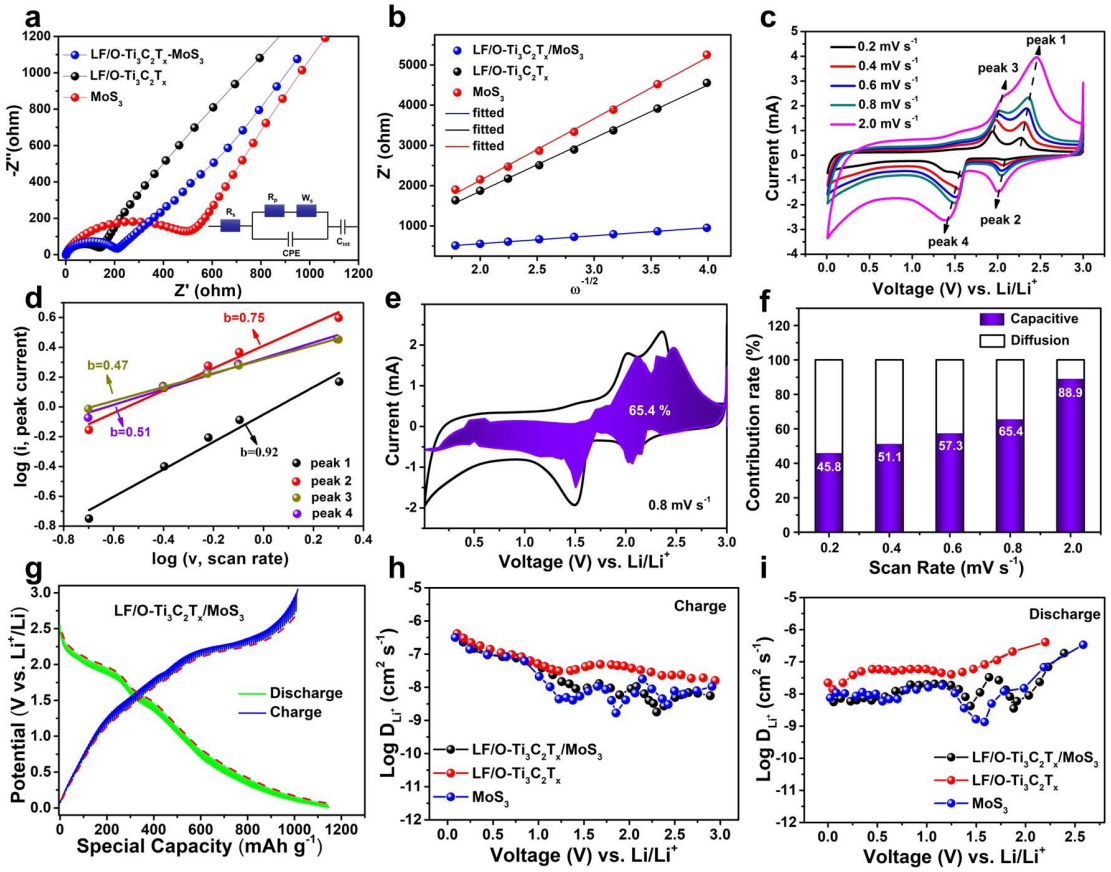

Fig. S22 Electrochemical kinetic analysis of LF/O-$Ti_3C_2T_x$/MoS_3 electrodes for LIBs: (a) EIS plots (the inset is the equivalent circuit), (b) relationship between Z' and $\omega^{-1/2}$ of three kinds of electrodes, (c) CV curves at different scan rates, (d) relationship between log *i* and log ν of cathodic and anodic peaks, (e) CV curves with capacitive contribution to the charge storage of 0.8 mV s^{-1}, (f) capacitive contribution rates at different scan rates, (g) GITT profiles (current pulse at 50 mA g^{-1} for 10 min followed by 1 h relaxation) and Li^+ diffusion coefficients at different voltages of (h) discharge and (i) charge process.

The electrochemical reaction kinetics of LF/O-$Ti_3C_2T_x$/MoS_3 was discussed. As observed in Fig. S22a, the semicircle diameter of LF/O-$Ti_3C_2T_x$/MoS_3 is much smaller than that of pure MoS_3, which indicates the small charge transfer impedance of LF/O-$Ti_3C_2T_x$/MoS_3 upon cycling. From Z' vs. $\omega^{-1/2}$ curves presented in Fig. S22b, the LF/O-$Ti_3C_2T_x$/MoS_3 exhibits the lowest slope than those of MoS_3 and LF/O-$Ti_3C_2T_x$, illustrating its fast lithium-ion transport kinetics in the interior of composite

electrode. The electrochemical mechanism of above electrode was also investigated to better understand the prominent lithium storage performance of LF/O-$Ti_3C_2T_x$/MoS_3. The CV curves at different scan rates show similar shapes with two pairs of cathodic and anodic peaks (Fig. S22c). The linear relationship of log i and log ν shown in Fig. S22d shows that the b values for the two pairs of oxidation and reduction peaks are 0.92, 0.75 and 0.47, 0.51, respectively. The high b values for peak 1 and peak 2 indicate that the overall charge storage process is a mixture of battery and capacitance behavior, while two b values approaching 0.5 for peak 3 and peak 4 show the diffusion controlled battery behavior. As observed in Fig. S22e, the proportion of capacitance contribution from the shaded area is 65.4% at 0.8 mV s^{-1}. Figure S22f further shows that the capacitance contribution gradually enhances with the increase of scan rate. When the scan rate increases to 2 mV s^{-1}, the capacitance contribution for LF/O-$Ti_3C_2T_x$/MoS_3 is as high as 88.9%, indicating the capacitance contribution will almost dominate the overall charge storage at high rates. GITT was also used to study the Li^+ reaction kinetics. A small overpotential can be observed from GITT profiles (Fig. S22g), and the Li^+ diffusion coefficients of LF/O-$Ti_3C_2T_x$/MoS_3 electrode is slightly smaller than that of LF/O-$Ti_3C_2T_x$ and comparative with that of MoS_3 (Figs. S22h and S22i), these values are higher than the other reported anode materials, indicating the good diffusion kinetics behavior of LF/O-$Ti_3C_2T_x$/MoS_3. The obvious decrease of Li^+ diffusion coefficients at discharge /charge voltage plateau suggests its bigger diffusion resistance during the electrochemical reaction process.

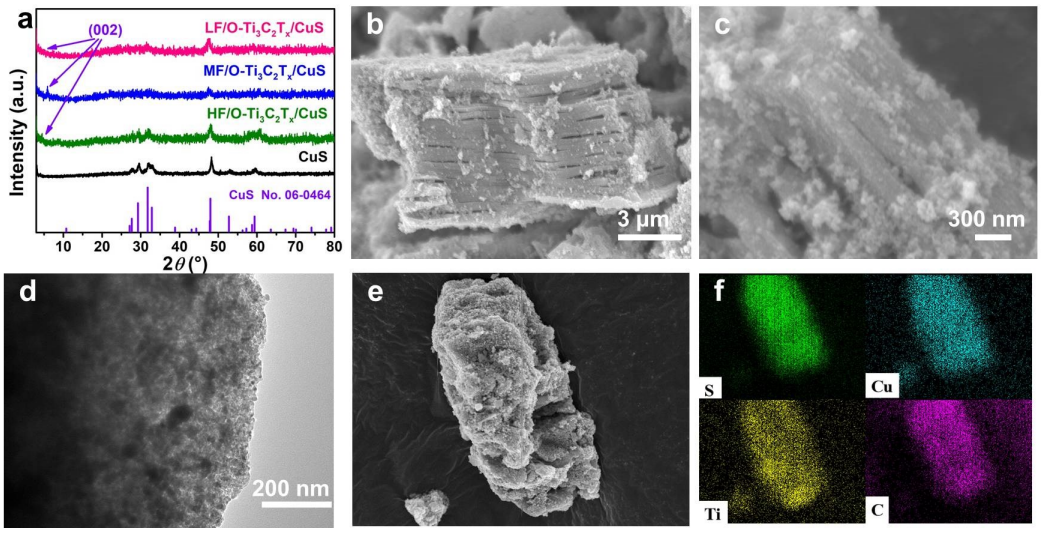

Fig. S23 Structures and morphologies of LF/O-$Ti_3C_2T_x$/CuS: (a) XRD patterns, (b) low magnified and (c) high magnified SEM images, (d) TEM image, (e, f) EDS elemental mapping.

Similar to LF/O-$Ti_3C_2T_x$/MoS_3, the dispersion of three titanium carbides was respectively added into a solution containing Cu^{2+} and S^{2-}. Afterwards, the temperature rose to 70 °C and the formed CuS crystal nucleus will deposit on the inner and outer surfaces of $Ti_3C_2T_x$. Figure S23a shows the XRD patterns of three $Ti_3C_2T_x$/CuS. As observed, two obvious diffraction peaks located at 31.78 ° and 47.94° are well matched with the (103) and (110) planes of hexagonal CuS (JCPDS No. 06-0464). Except for the diffraction peaks of CuS, two diffraction peaks located before 10° and around 60° can be observed in the XRD patterns of three composites, suggesting the existence of $Ti_3C_2T_x$. The weakness of (002) plane is probably attributed to the CuS loading on the surface of $Ti_3C_2T_x$. Figures S23b and S23c show the corresponding SEM images of LF/O-$Ti_3C_2T_x$/CuS. The magnified SEM image clearly shows that some small CuS nanoparticles are successfully loaded onto the inner and outer surfaces of LF/O-$Ti_3C_2T_x$. Furthermore, the SEM mapping further shows the uniform distribution of Ti, C, Cu, S and O elements (Figs. S23e-f). The atomic ratio of Cu and S is 1: 0.95, which is in agreement with CuS. In addition, the TEM image of LF/O-$Ti_3C_2T_x$/CuS is shown in Fig. S23d. As observed, the surface of LF/O-$Ti_3C_2T_x$ is uniformly coated by numerous CuS nanoparticles.

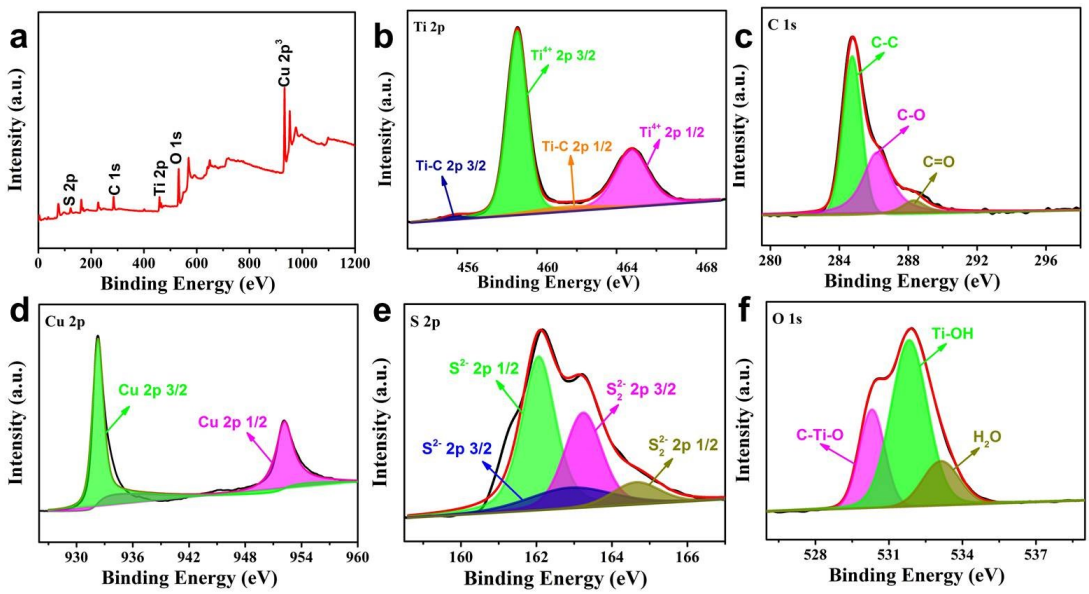

Fig. S24 XPS spectra of (a) survey spectrum, high resolution spectra of (b) Ti 2p, (c) C1s, (d) Cu 2p, (e) S 2p, (f) O 1s of LF/O-$Ti_3C_2T_x$/CuS.

The XPS survey spectrum shown in Fig. S24a reveals the existence of signals peaks of Cu, S, Ti, O and C elements, demonstrating the successful synthesis of LF/O-$Ti_3C_2T_x$/CuS. As for the Ti 2p (Fig. S24b), the Ti-C peaks can be fitted with two peaks located at 455.9 and 461.4 eV. The peaks situated at 459.0 and 464.7 eV can be assigned to the Ti-OH of Ti^{4+} 2p3/2 and Ti^{4+} 2p1/2 [S25]. Three peaks located at 284.8, 286.2 and 288.3 eV for C1s spectrum are assigned to C-C, C-O and C=O, respectively (Fig. S24c). Two primary peaks situated at 952.2 and 932.3 eV for Cu 2p spectrum are indexed to Cu^{2+} 2p1/2 and 2p3/2, respectively (Fig. S24d) [S26]. Two peaks located at 162.1 eV (S 2p3/2) and 162.9 eV (S 2p1/2) for S 2p spectrum are ascribed to S^{2-}, and the other two peaks at 163.2 eV and 164.6 eV for S 2p spectrum are correspond to the $S2^{4-}$ in Cu-S-S-Cu configuration (Fig. S24e) [S27]. Figure S24f shows the high-resolution XPS spectrum of O 1s, which can be fitted with three peaks centered at 530.3, 531.8 and 533.1 eV. The shoulder at 533.1 eV is due to H_2O. The peaks at 530.3 and 531.8 eV can be ascribed to C-Ti-O and Ti-OH [S28].

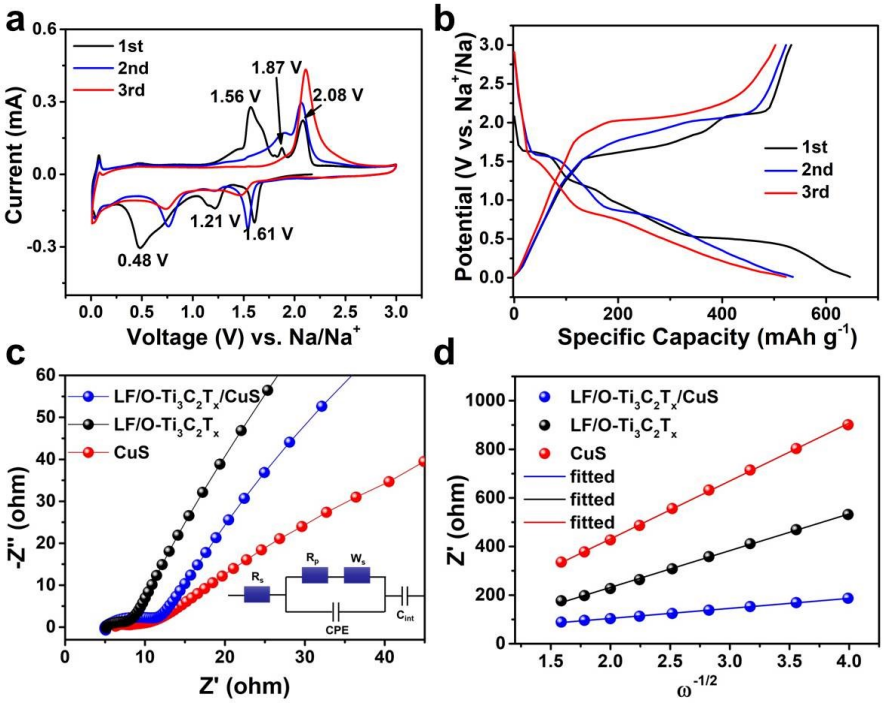

Fig. S25 (a) CV curves of LF/O-$Ti_3C_2T_x$/CuS at 0.1 mV s^{-1}, (b) charge/discharge curves, (c) EIS plots (the inset is the equivalent circuit), (d) relationship between Z' and $\omega^{-1/2}$ in the low frequency region of LF/O-$Ti_3C_2T_x$/CuS for SIBs.

Figure S25a first shows the CV curves. In the first negative scan, three cathode peaks located at 1.61, 1.21 and 0.48 V are attributed to the multi-step phase conversion of CuS to Na_2S and Cu as well as the formation of SEI film, respectively. In the first positive scan, two strong anodic peaks at around 1.56 and 2.08 V corresponds to the conversion from Cu and Na_2S to the intermediary $Na_\alpha Cu_\beta S_\gamma$, and then to $Cu_{2-x}S$. Also, the weak hump can be witnessed at 1.87 V, which may be caused by the side reaction of electrode and electrolyte [S29,S30]. However, the cathodic and anodic peaks for the second and subsequent cycles have obvious peak shift in comparison with those of first cycle due to the slow activation process [S31]. The voltage platforms in charge/discharge profiles of LF/O-$Ti_3C_2T_x$/CuS correspond well with those of redox peaks in CV curves (Fig. S25b). The discharge/charge capacity for the first cycle is 646/533 mAh g^{-1}, respectively, corresponding to a CE of 82%. The small charge transfer impedance (Fig. S25c), and lower slope than that of MoS_3 and LF/O-$Ti_3C_2T_x$ in Fig. S25d illustrate its fast electron and sodium-ion transport kinetics.

Table S6 The sodium storage performance comparison of CuS related composites.

Samples	Current density (mA g^{-1})	Cycle numbers	Specific capacity (mAh g^{-1})	Ref.
PNL-CuS	100	100	522	[S29]
CuS NWs@NC	200	100	571	[S31]
CuS microspheres	200	200	162	[S32]
hollow CuS	100	100	361	[S33]
CuS-RGO	100	50	392	[S34]
	1000	450	345	
LF/O-$Ti_3C_2T_x$/CuS	500	200	597	This work
	2000	400	553	

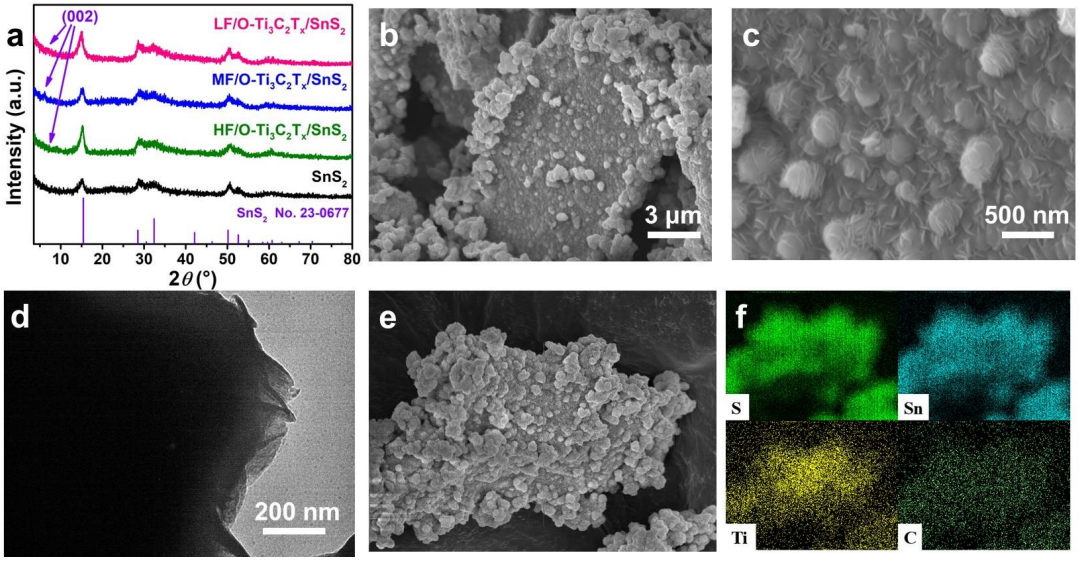

Fig. S26 The structures and morphologies of LF/O-$Ti_3C_2T_x$/SnS_2: (a) XRD patterns, (b) low magnified, (c) high magnified SEM images, (d) TEM image, (e, f) EDS elemental mapping.

Consistent with LF/O-$Ti_3C_2T_x$/MoS_3 and LF/O-$Ti_3C_2T_x$/CuS, the dispersion of three kinds of titanium carbides was respectively added into a solution containing Sn^{4+} and TAA. The formed SnS_2 crystal nucleus will deposit on the inner and outer surfaces of titanium carbide under a temperature of 60 ^oC. As presented in the XRD patterns (Fig. S26a), all the diffraction peaks for three composites located at 15.03^o, 28.20^o, 32.12^o, 49.96^o and 52.45^o are well matched with hexagonal SnS_2 (JCPDS No. 23-0677). Two other weak diffraction peaks located before 10^o and around 60^o suggest the existence of $Ti_3C_2T_x$. The magnified SEM images in Figs. S26b and S26c clearly show that some SnS_2 nanospheres and nanosheets are attached on the surface of LF/O-$Ti_3C_2T_x$ layers, suggesting the successful preparation of LF/O-$Ti_3C_2T_x$. SEM mapping further shows the uniform distribution of Ti, C, Sn, S and O elements (Fig. S26e and S26f). The atomic ratio of Sn and S is 1: 2.1, which is in agreement with SnS_2. The related TEM image of LF/O-$Ti_3C_2T_x$/SnS_2 in Fig. S26d shows that the surface of LF/O-$Ti_3C_2T_x$ is uniformly coated by SnS_2 nanosheets.

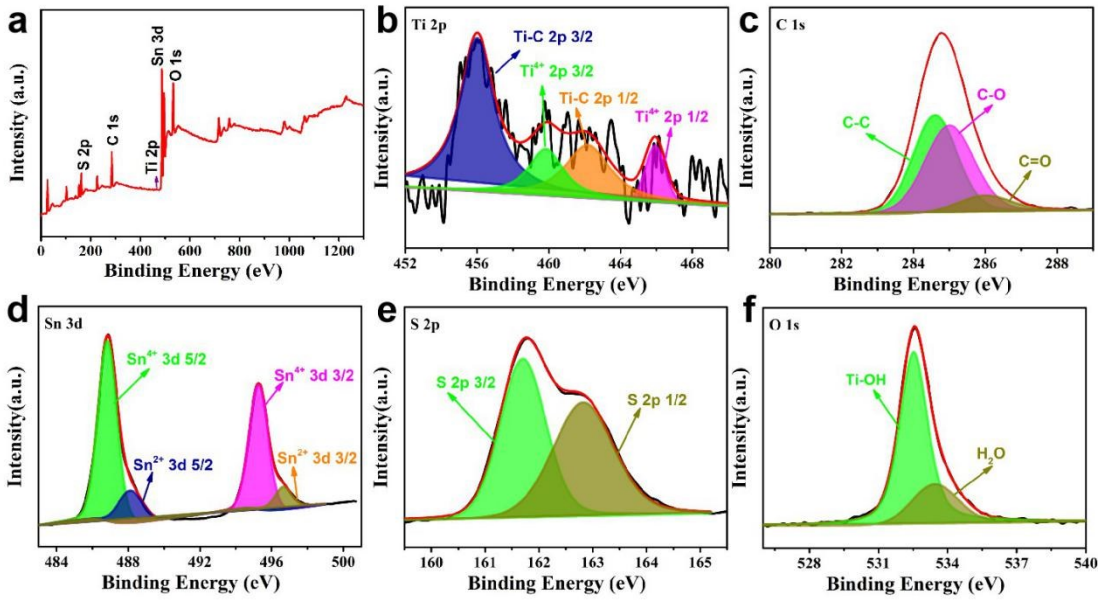

Fig. S27 XPS spectra of (a) survey spectrum, high resolution spectra of (b) Ti 2p, (c) C1s, (d) Sn 3d, (e) S 2p, (f) O 1s of LF/O-$Ti_3C_2T_x$/SnS_2.

The XPS survey spectrum of LF/O-$Ti_3C_2T_x/SnS_2$ shown in Fig. S27a reveals the existence of signals peaks of Sn, S, Ti, O and C elements, demonstrating the successful synthesis of LF/O-$Ti_3C_2T_x/SnS_2$. As for the Ti 2p (Fig. S27b), the Ti-C peaks can be fitted with two peaks located at 456.0 and 462.1 eV. The peaks situated at 459.7 and 465.9 eV can be assigned to the Ti-OH of Ti^{4+} 2p3/2 and Ti^{4+} 2p1/2 [S25]. Three peaks located at 284.6, 285.0 and 286 eV for C1s spectrum are attributed to C-C, C-O and C=O, respectively (Fig. S27c). In the spectrum of Sn 3d exhibited in Fig. S27d, two primary peaks situated at 488.1 and 496.6 eV are indexed to Sn^{4+} 3d5/2 and 3d3/2, respectively. The other two weak peaks at 486.8 and 495.2 eV are assigned to Sn^{2+} 3d5/2 and Sn^{2+} 3d3/2, respectively [S35,S36]. As shown in Fig. S27e, the two peaks located at 162.8 eV (S 2p1/2) and 161.7 eV (S 2p3/2) for S 2p spectrum are ascribed to S^{2-} [S37]. Figure S27f shows the high-resolution XPS spectrum of O 1s, the two peaks centered at 533.4 and 532.5 eV are attributed to H_2O and Ti-OH, respectively [S28].

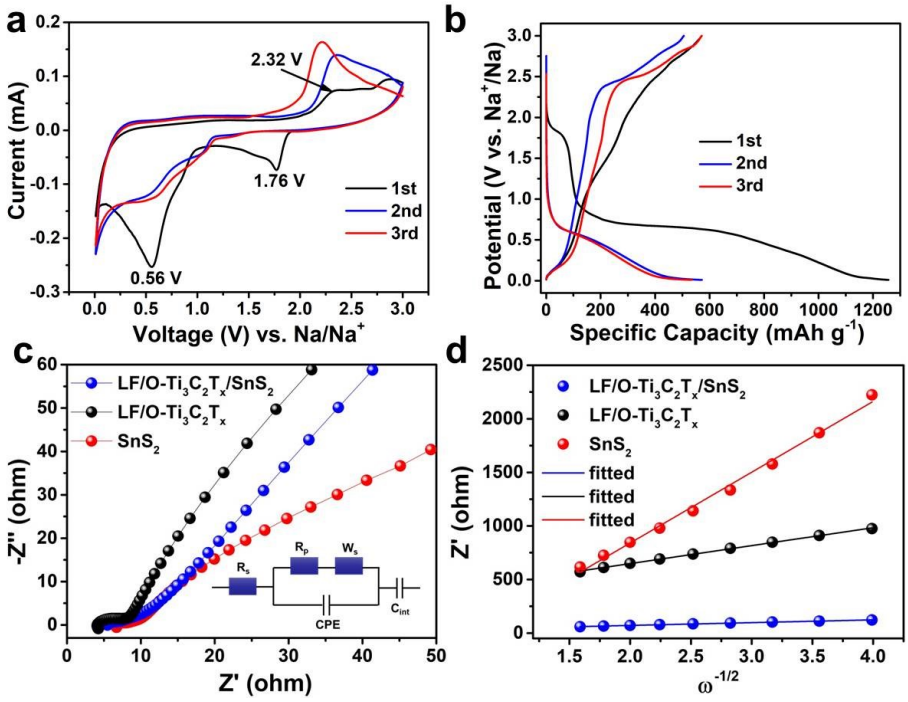

Fig. S28 (a) CV curves of LF/O-$Ti_3C_2T_x$/SnS_2 at 0.1 mV s^{-1}, (b) charge/discharge curves, (c) EIS plots (the inset is equivalent circuit), (d) relationship between Z' and $\omega^{-1/2}$ in the low frequency region of LF/O-$Ti_3C_2T_x$/SnS_2 for SIBs.

Figure S28a shows the CV curves at 0.1 mV s^{-1} of LF/O-$Ti_3C_2T_x$/SnS_2, which corresponds well with the charge/discharge profiles (Fig. S28b). The cathode peak located at 1.76 V for the first cycle is assigned as insertion of Na^+ into SnS_2 layers to form Na_xSnS_2, and this peak disappears in the following cycles, suggesting the intercalation reaction is irreversible. The strong peak of 0.56 V originates from the conversion reaction of SnS_2 to form Sn and Na_2S and further alloying process of Sn to generate final $Na_{3.75}Sn$ phase as well as the formation of SEI film. The anodic peak at around 2.32 V for the initial cycle corresponds to the extraction reaction of sodium ion from Na_xSn and subsequent oxidation of Sn to SnS_2 [S38]. The cathodic and anodic peaks shift for the second and third cycles is resulted from the irreversible structural transformation [S39,S40]. The EIS results are shown in Figs. S28c and S28d illustrate the fast electron and ion transport kinetics of LF/O-$Ti_3C_2T_x$/SnS_2.

Table S7 The sodium storage performance comparison of SnS_2 related composites.

Samples	Current density ($mA\ g^{-1}$)	Cycle numbers	Specific capacity ($mAh\ g^{-1}$)	Ref.
SnS_2@N,S-GA	20	50	527	[4]
SnS_2/GCA	200	100	535	[12]
MXene/SnS_2	100	200	322	[41]
3D-GNS/SnS_2	1000	1000	385	[S37]
P-SnS_2@TiC/C	200	200	681	[S39]
ZnS/SnS_2@N/S C	1000	120	537	[S41]
SnS_2 NP/TiO_2@C	500	100	543	[S42]
	2000	100	413	
SnS_2@C	200	200	626	[S43]
SnS_2/NS-CNT	200	80	417	[S44]
SnS/SnS_2@CC	1000	500	455	[S45]
SnS_2/Sb_2S_3@rGO	200	100	642	[S46]
	1000	400	480	
SnS_2/C	50	100	600	[S47]
SnS_2/RGO	200	100	841	[S48]
LF/O-$Ti_3C_2T_x$/SnS_2	500	100	766	This work
	2000	400	574	

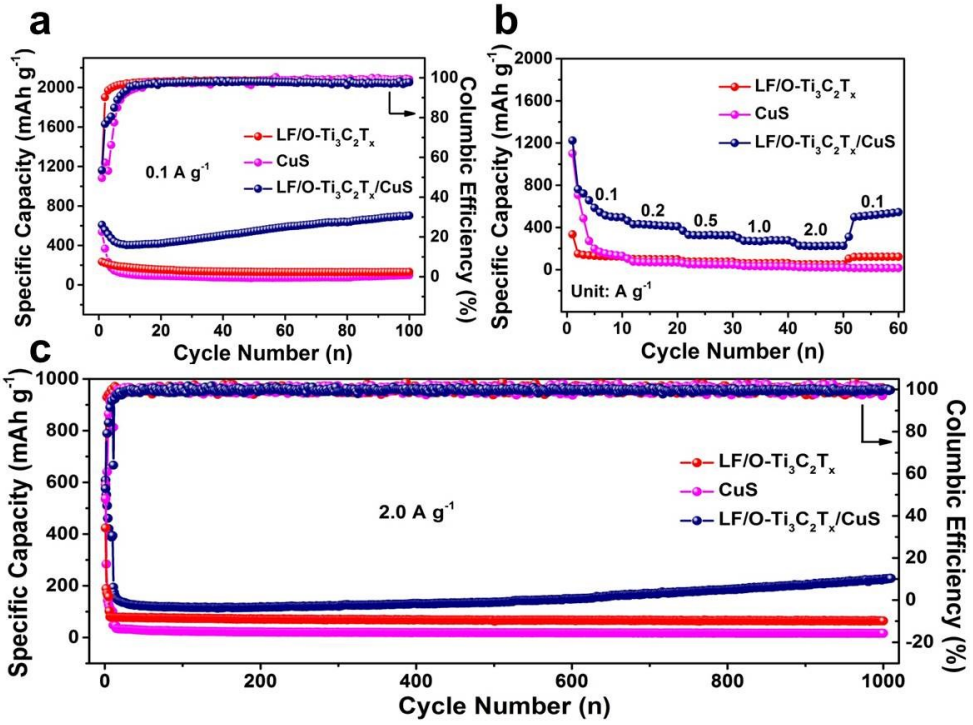

Fig. S29 (a) cycling performance, (b) rate capabilities and (c) high-rate cycling performance of LF/O-$Ti_3C_2T_x$/CuS for LIBs.

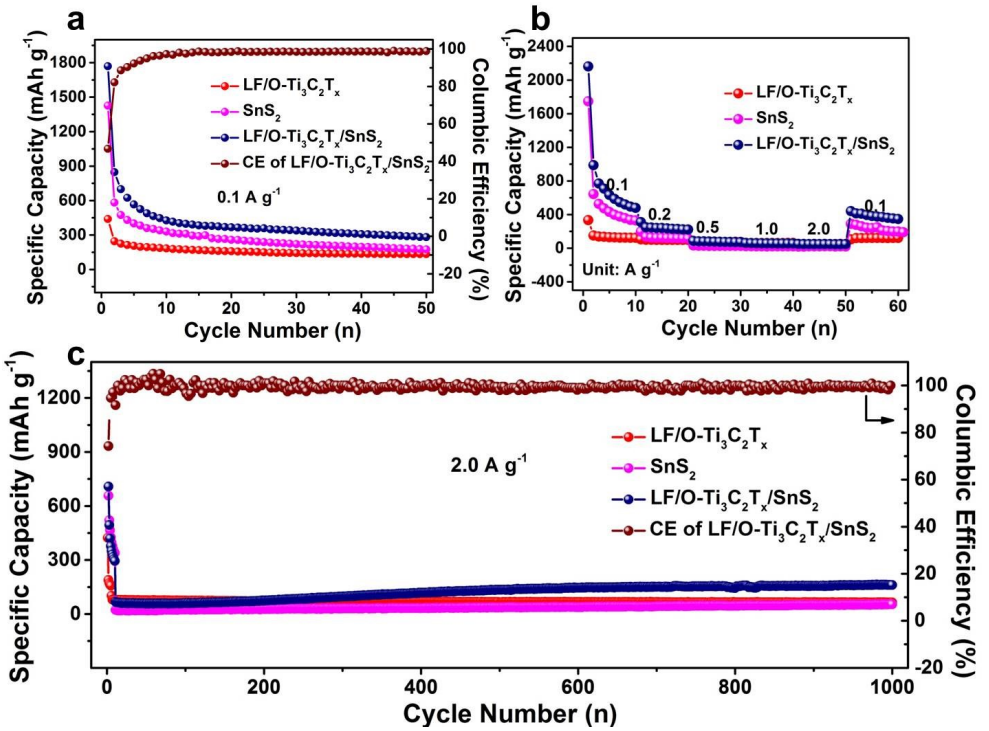

Fig. S30 (a) cycling performance, (b) rate capabilities and (c) high-rate cycling performance of LF/O-$Ti_3C_2T_x$/SnS_2 for LIBs.

Supplementary References

[S1] G. Xu, L. Yang, X. Wei, J. Ding, J. Zhong and P. K. Chu, *Adv. Funct. Mater*., 2016, **26**, 3349-3358.

[S2] H. Ye, L. Wang, S. Deng, X. Zeng, K. Nie, P. N. Duchesne, B. Wang, S. Liu, J. Zhou, F. Zhao, N. Han, P. Zhang, J. Zhong, X. Sun, Y. Li, Y. Li and J. Lu, *Adv. Energy Mater*., 2017, **7**, 1601602.

[S3] L. Cao, X. Liang, X. Ou, X. Yang, Y. Li, C. Yang, Z. Lin and M. Liu, *Adv. Funct. Mater*., 2020, **30**, 1910732.

[S4] A. Cheng, H. Zhang, W. Zhong, Z. Li, D. Cheng, Y. Lin, Y. Tang, H. Shao and Z. Li, *Carbon*, 2020, **168**, 691-700.

[S5] W. Zhang, H. Zhou, Z. Huang, S. Li, C. Wang, H. Li, Z. Yan, T. Hou and Y. Kuang, *J. Energy Chem*., 2020, **49**, 307-315.

[S6] S. Anwer, Y. Huang, B. Li, B. Govindan, K. Liao, J. C. W, F. Wu, R. Chen and L. Zheng, *ACS Appl. Mater. Interfaces*, 2019, **11**, 22323-22331.

[S7] G. K. Veerasubramani, M.-S. Park, G. Nagaraju and D.-W. Kim, *J. Mater. Chem. A*, 2019, **7**, 24557-24568.

[S8] Y. Li, R. Zhang, W. Zhou, X. Wu, H. Zhang and J. Zhang, *ACS Nano*, 2019, **13**, 5533-5540.

[S9] D. Sun, D. Ye, P. Liu, Y. Tang, J. Guo, L. Wang and H. Wang, *Adv. Energy Mater*., 2018, **8**, 1702383.

[S10] G. Wang, X. Bi, H. Yue, R. Jin, Q. Wang, S. Gao and J. Lu, *Nano Energy*, 2019, **60**, 362-370.

[S11] J. H. Peng, X. Z. Chen, W. J. Ong, X. Zhao and N. Li, *Chem*., 2019, **1**, 18–50.

[S12] W. Zheng, P. Zhang, J. Chen, W. B. Tian, Y. M. Zhang and Z. M. Sun, *J. Mater. Chem. A*, 2018, **6**, 3543–3551.

[S13] Z. Lin, D. Sun, Q. Huang, J. Yang, M. W. Barsoum and X. Yan, *J. Mater. Chem. A*, 2015, **3**, 14096–14100.

[S14] G. Du, M. Tao, W. Gao, Y. Zhang, R. Zhan, S. Bao and M. Xu, *Inorg. Chem.*

Front., 2019, **6**, 117-125.

[S15] Z. Ma, X. Zhou, W. Deng, D. Lei and Z. Liu, *ACS Appl. Mater. Interfaces*, 2018, **10**, 3634–3643.

[S16] Y. S. Wang, Y. Y. Li and S. P. Zhuo, *J. Mater. Chem. A*, 2018, **6**, 11189–11197.

[S17] F. Wang, Z Wang and C Yang, *J. Mater. Sci*., 2017, **52**, 3556–3565.

[S18] P. Zhang, D. Wang, Q. Zhu, N. Sun, F. Fu and B. Xu, *Nano-Micro Lett.*, 2019, **11**, 81.

[S19] S. Zhang, X.Y. Li, W. Yang, H. Tian, Z. Han , H. Ying, G. Wang and W. Han, *ACS Appl. Mater. Interfaces*, 2019, **11**, 42086–42093.

[S20] X. Sun, K. Tan, Y. Liu, J. Zhang, D. Deni, F. Zaman, L. Hou and C. Yuanet, *Nanoscale*, 2019, **11**, 16755–16766.

[S21] Y. Huang, H. Yang, Y. Zhang, Y. Zhang, Y. Wu, M. Tian, P. Chen, R. Trout, Y. Ma, T. Wu, Y. Wu and N. Liu, *J. Mater. Chem. A*, 2019, **7**, 11350–11356.

[S22] J. Ai, Y. Lei, S. Yang, C. Lai and Q. Xu, *Chem. Eng. J*., 2019, **357**, 150–158.

[S23] M. Lu, H. Li, W. Han, Y. Wang, W. Sh, J. Wang, H. Chen, H. Li, B. Zhang, W. Zhang and W. Zheng, *Nanoscale*, 2019, **11**, 15037–15042.

[S24] C. Wang, X Zhu, Y. Mao, F. Wang, X. Gao, S. Qiu, S. Leb and K.N. Sun, *Chem. Commun*., 2019, **55**, 1337–1340.

[S25] X. Wu, Z. Wang, M. Yu, L. Xiu and J. Qiu, *Adv. Mater*., 2017, **29**, 1607017.

[S26] S. Li, Z. Ge, B. Zhang, Y. Yao and H. Wang, *Appl. Surf. Sci*., 2016, **384**, 272-278.

[S27] S.I. Raj and A. Jaiswal, *J. Photoch. Photobio. A*., 2021, **410**, 113185.

[S28] Z. Pan, F. Cao, X. Hu and X. Ji, *J. Mater. Chem. A*, 2019, **7**, 8984-8992.

[S29] D. Yu, M. Li, T. Yu, C. Wang, Y. Zeng, X. Hu, G. Chen, J. Yang and F. Du, *J. Mater. Chem. A*, 2019, **7**, 10619-10628.

[S30] R. Zhao, H. Di, X. Hui, D. Zhao, R. Wang, C. Wang and L. Yin, *Energ. Environ. Sci*., 2020, **13**, 246–257.

[S31] D. Zhao, M. Yin, C. Feng, K. Zhan, Q. Jiao, H. Li and Y. Zhao, *ACS Sustain. Chem. Eng*., 2020, **8**, 11317-11327.

[S32] H. Li, Y. Wang, J. Jiang, Y. Zhang, Y. Peng and J. Zhao, *Electrochim. Acta*, 2017, **247**, 851-859.

[S33] L. Wu, J. Gao, Z. Qin, Y. Sun, R. Tian, Q. Zhang and Y. Gao, *J. Power Sources*, 2020, **479**, 228518.

[S34] J. Li, D. Yan, T. Lu, W. Qin, Y. Yao and L. Pan, *ACS Appl. Mater. Interfaces*, 2017, **9**, 2309-2316.

[S35] H. Tang, R. Guo, M. Jiang, Y. Zhang, X. Lai, C. Cui, H. Xiao, S. Jiang, E. Ren and Q. Qin, *J. Power Sources*, 2020, **462**, 228152.

[S36] S. Guan, T. Wang, X. Fu, L. Fan and Z. Peng, *Appl. Surf. Sci*., 2020, **508**, 145241.

[S37] Z. Sang, X. Yan, D. Su, H. Ji, S. Wang, S. Dou and J. Liang, *Small*, 2020, **16**, 2001265.

[S38] Y. Zhang, P. Zhu, L. Huang, J. Xie, S. Zhang, G. Cao and X. Zhao, *Adv. Funct. Mater*., 2015, **25**, 481-489.

[S39] Y. Shen, S. Deng, P. Liu, Y. Zhang, Y. Li, X. Tong, H. Shen, Q. Liu, G. Pan, L. Zhang, X. Xia and J. Tu, *Small*, 2020, **16**, 2004072.

[S40] X. Shi, S. Chen, H. Fan, X. Chen, D. Yuan, Q. Tang, A. Hu, W. Luo and H. Liu, *ChemSusChem*, 2019, **12**, 4046-4053.

[S41] L. Cao, B. Zhang, X. Ou, C. Wang, C. Peng and J. Zhang, *Small*, 2019, **15**, 1804861.

[S42] X. Hu, Q. Peng, T. Zeng, B. Shang, X. Jiao and G. Xi, *Chem. Eng. J*., 2019, **363**, 213-223.

[S43] S. Li, Z. Zhao, C. Li, Z. Liu and D. Li, *Nano-Micro Lett.*, 2019, **11**, 14.

[S44] Z. Liu, A. Daali, G. L. Xu, M. Zhuang, X. Zuo, C. J. Sun, Y. Liu, Y. Cai, M. D. Hossain, H. Liu, K. Amine and Z. Luo, *Nano Lett*., 2020, **20**, 3844-3851.

[S45] J. Lu, S. Zhao, S. Fan, Q. Lv, J. Li and R. Lv, *Carbon*, 2019, **148**, 525-531.

[S46] S. Wang, S. Liu, X. Li, C. Li, R. Zang, Z. Man, Y. Wu, P. Li and G. Wang, *Chem*., 2018, **24**, 3873-3881.

[S47] J. Wang, C. Luo, J. Mao, Y. Zhu, X. Fan, T. Gao, A. C. Mignerey and C. Wang, *ACS Appl. Mater. Interfaces*, 2015, **7**, 11476-11481.

[S48] B. Zhao, D. Song, Y. Ding, W. Li, Z. Wang, Y. Jiang and J. Zhang, *Electrochim. Acta*, 2020, **354**, 136730.